

# Optical Manipulation of the Charge Density Wave state in $\text{RbV}_3\text{Sb}_5$

Yuqing Xing<sup>1†</sup>, Seokjin Bae<sup>1†</sup>, Ethan Ritz<sup>2</sup>, Fan Yang<sup>2</sup>, Turan Biro<sup>2</sup>, Andrea N. Capa Salinas<sup>3</sup>,  
Brenden R. Ortiz<sup>3</sup>, Stephen D. Wilson<sup>3</sup>, Ziqiang Wang<sup>4</sup>, Rafael M. Fernandes<sup>5</sup>, Vidya  
Madhavan<sup>1\*</sup>

<sup>1</sup> Department of Physics and Materials Research Laboratory, University of Illinois Urbana-Champaign, Urbana, IL 61801, USA.

<sup>2</sup> Department of Chemical Engineering and Materials Science, University of Minnesota, Minneapolis, Minnesota 55455, USA

<sup>3</sup> Materials Department, University of California Santa Barbara, Santa Barbara, California 93106, USA

<sup>4</sup> Department of Physics, Boston College, Chestnut Hill, Massachusetts 02467, USA

<sup>5</sup> School of Physics and Astronomy, University of Minnesota, Minneapolis, Minnesota 55455, USA

**Broken time-reversal symmetry in the absence of spin order indicates the presence of unusual phases such as orbital magnetism and loop currents<sup>1–4</sup>. The recently discovered family of kagome superconductors  $\text{AV}_3\text{Sb}_5$  (A = K, Rb, or Cs)<sup>5,6</sup>, hosting an exotic charge-density wave (CDW) state, has emerged as a strong candidate for this phase. While initial experiments suggested that the CDW phase breaks time-reversal symmetry<sup>7–14</sup>, this idea is being intensely debated due to conflicting experimental data<sup>15–17</sup>. In this work we use laser-coupled scanning tunneling microscopy (STM) to study  $\text{RbV}_3\text{Sb}_5$ . STM data shows that the Fourier intensities of all three CDW peaks are different, implying that the CDW breaks rotational and mirror symmetries. By applying linearly polarized light along high-symmetry directions, we show that the relative intensities of the CDW peaks can be reversibly switched, implying a substantial electrostriction response, indicative of strong non-linear electron-phonon coupling. A similar CDW intensity switching is observed with perpendicular magnetic fields, which implies an unusual piezo-magnetic response that, in turn, requires time-reversal symmetry-breaking. We show that the simplest CDW that satisfies these constraints and reconciles previous seemingly contradictory experimental data is an out-of-phase combination of bond charge order and loop currents that we dub congruent CDW flux phase. Our laser-STM data opens the door to the possibility of dynamic optical control of complex quantum phenomenon in correlated materials.**

†These authors contributed equally to this work

\*Correspondence to: [vm1@illinois.edu](mailto:vm1@illinois.edu)

Kagome lattice compounds provide an ideal platform to study novel states of quantum matter resulting from the interplay between topology, geometric frustration, and electron correlations<sup>18–21</sup>. This class of materials includes magnetic metals such as  $\text{Fe}_3\text{Sn}_2$ ,  $\text{Co}_3\text{Sn}_2\text{S}_2$ , and  $\text{TbMn}_6\text{Sn}_6$ , which host massive Dirac fermions<sup>22–24</sup>, magnetic topological Weyl points<sup>25,26</sup>, and Chern magnetism<sup>27</sup>, as well as the recently discovered non-magnetic superconductors  $\text{AV}_3\text{Sb}_5$  (where A=K, Rb, Cs)<sup>5,6</sup>, which exhibit a landscape of exotic correlated and topological states in a complex phase diagram<sup>28–32</sup>. Besides superconductivity, this family of materials hosts a CDW phase that not only breaks additional lattice symmetries such as rotation<sup>15</sup> and mirror<sup>7</sup>, but may also break time-reversal (TR) symmetry<sup>7–14</sup>. The latter is particularly intriguing since broken TR symmetry not driven by spins suggests orbital magnetism. The particular type of orbital magnetism proposed for the kagome compounds is that of staggered circulating orbital currents<sup>7</sup>, resembling other states that have been suggested for many decades in the context of quantum anomalous Hall states<sup>1</sup> and correlated systems<sup>2–4</sup>. In the case of  $\text{AV}_3\text{Sb}_5$ , experiments that are consistent with TR symmetry-breaking include initial scanning tunneling microscopy measurements that detected a magnetic-field sensitive CDW intensity pattern<sup>7</sup>; muon spin-rotation ( $\mu\text{SR}$ ) experiments that showed a sharp and magnetic-field enhanced increase in the relaxation rate below the CDW transition temperature<sup>8–10</sup>; and optical measurements that reported the onset of a spontaneous polar Kerr rotation and circular dichroism at the CDW transition<sup>11,12,14</sup>. These observations have motivated various theoretical studies of the so-called flux-CDW phase in kagome metals, which relies on electronic correlations as the driving force behind this exotic instability<sup>33–38</sup>. However, the scenario of TR symmetry-breaking CDW in the kagome superconductors has been challenged by recent STM measurements that did not reproduce the magnetic-field induced switching of the CDW intensities<sup>15</sup> and by Sagnac interferometer measurements that did not find spontaneous Kerr rotation in the CDW state<sup>16,17</sup>. Pinning down the nature of the CDW phase is vitally important not only to demonstrate or rule out the realization of an exotic flux-CDW phase with loop currents, but also because superconductivity in these materials emerges deep within the CDW phase.

In this work we study the electric and magnetic field responses of the CDW phase of the kagome superconductor  $\text{RbV}_3\text{Sb}_5$  with a scanning tunneling microscope that is coupled to

laser light. Within the class of  $AV_3Sb_5$  ( $A = K$ ,  $Rb$ , or  $Cs$ ) materials, studying  $RbV_3Sb_5$  is advantageous because it avoids the complexities associated with the co-existence of different types of bond distortions that are seen in the more commonly studied  $CsV_3Sb_5$  compound<sup>39–41</sup>.  $RbV_3Sb_5$  has a layered hexagonal crystal structure (lattice constants  $a = 5.47 \text{ \AA}$  and  $c = 9.1 \text{ \AA}$ ) which consists of the V-Sb kagome layer sandwiched between two Sb honeycomb layers and separated by an alkaline Rb hexagonal layer (Fig. 1a,b)<sup>5</sup>. For these studies,  $RbV_3Sb_5$  samples were cleaved in-situ in ultra-high vacuum at  $\sim 90 \text{ K}$  before inserting into the STM head. Cleavage naturally occurs between the Rb and Sb planes. Since the Rb atoms are extremely weakly bonded to each other and to the Sb plane, statistically only half of the Rb atoms are left behind on each cleave surface. This results in the exposure of the Sb honeycomb layer with a random sprinkling of Rb adatoms. Fortunately, the loosely held Rb adatoms can be 'swept away' with the STM tip (Extended Data Fig. 1), allowing us to directly probe a clean Sb surface. Figure 1c and 1d show the topographic image and the Fourier transform (FT) of such a cleaned surface. High resolution topography shows the Sb honeycomb lattice (Extended Data Fig. 2a) with a lattice constant of  $\sim 5.4 \text{ \AA}$  (Extended Data Fig. 2b), consistent with the crystal structure determined by previous experiments<sup>42–44</sup>. The Fourier transform reveals a rich pattern of charge order and Friedel oscillations (marked as  $Q_F$ ). The three Bragg peaks in the three symmetry-related  $\Gamma$ -M directions are labelled  $Q_{B1}$ ,  $Q_{B2}$ , and  $Q_{B3}$  and the  $2a_0 \times 2a_0$  CDW peaks along these directions are labelled  $Q_1$ ,  $Q_2$ , and  $Q_3$  respectively. The Fourier peak labeled by  $Q_{4a_0}$  corresponds to the unidirectional charge order<sup>42,43,45</sup> with a period of  $\sim 4a_0$  along the  $Q_2$  direction, which was also observed in previous STM measurements but not in X-ray experiments.

A closer look at the FT shown in Fig. 1d reveals a few interesting features. First, the intensity of the  $Q_2$  peak (henceforth labelled  $I_2$ ) is significantly higher than the intensity of both  $Q_1$  ( $I_1$ ) and  $Q_3$  ( $I_3$ ). This can be seen by comparing the line profiles along three Bragg peak directions as shown in Fig. 1e, and indicates the breaking of threefold rotational symmetry of the  $2a_0 \times 2a_0$  CDW, consistent with previous literature<sup>7,15,42,43,46</sup>. Theoretically, this rotation symmetry breaking has been attributed to either the stacking between Star-of-David and tri-hexagonal patterns of the CDW along the c-axis or to admixture of the bond-CDW with a flux phase<sup>35,36,38,47</sup>. Second, we find that  $I_1$  and  $I_3$  are also different, which indicates that vertical and diagonal mirror symmetries are also broken such that all three CDW peaks have different

intensities. We will show later in the paper that the difference between  $I_1$  and  $I_3$  is likely due to small residual strain. The lack of mirror planes perpendicular to the kagome layer gives rise to two different senses of handedness in the CDW peak intensities, which were referred to as “chiral” in previous STM studies<sup>7,43</sup>, when they appeared to be switchable by applying a c-axis magnetic field. To understand the origin of this remarkable phenomenon, we study the response of the CDW to a different type of electromagnetic probe, i.e., light.

A schematic of our laser-STM setup is shown in Fig. 2a. A burst ( $2 \times 10^5$  shots at 100 kHz repetition rate) of linearly polarized, ultrafast (250 fs), near-infrared (1025 nm) laser pulses at a fluence of  $0.39 \text{ mJ/cm}^2$  (unless otherwise mentioned) is used to illuminate the sample surface. The polarization direction of the electric field is controlled (rotated) by the half-wave plate to align with various lattice directions of interest. The laser beam is focused on an  $\sim 50 \mu\text{m}$  sized spot that covers the area under the STM tip. The angle between the surface normal and the beam propagation is 55 degrees. The tip is retracted  $70 \mu\text{m}$  just before laser illumination and is repositioned on the same area after illumination. More details about laser parameters, optics setup, and laser-STM experimental procedures can be found in Methods and Extended Data Fig. 3.

Figure 2 shows the FT of the topography and the  $2a_0 \times 2a_0$  CDW peak intensities before and after illumination. In this study, the laser electric field ( $\mathbf{E}$ ) is oriented along the in-plane  $\Gamma$ -M directions pointing towards either  $\mathbf{Q}_1$  or  $\mathbf{Q}_3$  (we henceforth label light with  $\mathbf{E} \parallel \mathbf{Q}_1$  as  $\mathbf{E}_1$  and  $\mathbf{E} \parallel \mathbf{Q}_3$  as  $\mathbf{E}_3$ ). We note here that the directions  $\mathbf{E}_1$  and  $\mathbf{E}_3$  are along the honeycomb Sb-Sb nearest neighbor direction in Q-space and therefore along the V-V nearest neighbor directions in real space. Before illumination,  $I_1 > I_3$  such that the sequence of the three CDW intensities from brightest to least bright goes clockwise (Fig. 2c,d). Strikingly, we find that after illumination with  $\mathbf{E}_3$  (Fig. 2e,f),  $I_1 < I_3$  which results in a counterclockwise intensity sequence. We further find that this light-induced CDW intensity change is reversible. Illuminating the sample with  $\mathbf{E}_1$  reverses the sequence of intensities again, leading to  $I_1 > I_3$  (Fig. 2g,h). We note that due to the inherent broken rotational symmetry of the CDW,  $I_2$  always remains the strongest in this field of view, so for the rest of this paper we will not discuss  $I_2$ .

To demonstrate the robustness and repeatability of the light induced switching, we show the results of a series of laser illuminations with light polarized either along  $\mathbf{E}_1$  or  $\mathbf{E}_3$  as shown in

Fig. 3a. Here we plot the relative intensity  $I_r = (I_1 - I_3)/((I_1 + I_3)/2)$  where a positive/negative  $I_r$  (marked in red or blue) corresponds to a stronger  $I_1$  or  $I_3$  respectively. Plotting  $I_r$  rather than the absolute intensity values allows us to eliminate arbitrary intensity changes in the overall FT between measurements. Initially, before laser illumination,  $I_1 > I_3$ , leading to a positive  $I_r$ . After laser illumination with  $E_3$ ,  $I_r$  becomes negative meaning that now  $I_1 < I_3$ . Amazingly, as we track  $I_r$  through a sequence of light pulses, we find a one-to-one correspondence between the sign of  $I_r$  and the direction of the electric field, as shown in Fig. 3a (also see Fig. 3b for the full statistics of 35 different illuminations in an arbitrary sequence). This means that shining light along  $E_1$  or  $E_3$  always makes the intensity of the corresponding CDW peak stronger. There are three other important points to make. First, the fact that the intensities can be controlled with laser illumination unequivocally proves that the intensity differences are a feature of the sample and not measurement artifacts. Second, we find that the switching is independent of the number of pulses in an illumination and occurs even within the single pulse limit as shown in Fig. 3f. Finally, the laser induced switching requires a critical fluence of  $\sim 0.39 \text{ mJ/cm}^2$  (Fig. 3e). This threshold effect indicates a double well free energy landscape in the presence of light as we discuss later in the paper.

A CDW order is typically intertwined with a lattice distortion resulting from the displacements of the atoms from their original positions above the CDW transition temperature. Remarkably, we are able to directly observe such intertwining in our data by tracking the positions in Fourier space of both the Bragg and CDW peaks as the electric field is switched. To see this, we extract the ratio between the magnitude of the Bragg vectors i.e.,  $Q_r = |Q_{B1}|/|Q_{B3}|$  as an indicator of the change in the relative lattice constants after laser illumination (see Extended Data Fig. 4 for further details on how  $Q_B$  is measured). Fig. 3c shows that  $Q_r$  displays the same pattern as the relative CDW intensity  $I_r$  shown in Fig. 3a. In particular, the ratio  $Q_r$  increases when illuminating with  $E_1$ , which means that when  $I_1$  increases,  $Q_{B1}$  increases. Conversely, when  $I_3$  increases,  $Q_r$  decreases which means that  $Q_{B3}$  increases. Concomitantly with the change in the Bragg momentum, the ratio between the CDW peak positions also changes (Extended Data Fig. 5) such that the  $2a_0 \times 2a_0$  CDW remains commensurate after laser illumination (Fig. 3d). In other words, while the absolute value of the CDW wave-vector changes, its coordinates with respect to the reciprocal lattice vectors remain unchanged. These combined observations suggest a strong electron-phonon coupling in this system and

establish that the light-induced intensity-change can be attributed to a sizable electro-striction response of the CDW state.

The surprising laser-induced switching of CDW intensities observed here is similar to the previously reported magnetic field switching of the relative CDW intensities<sup>7,43</sup>. To obtain a comprehensive picture, it is important to ascertain if a similar magnetic field induced switching occurs in our samples. Shown in Fig. 4a is an STM topography in a magnetic field (+ 2 T). First, even with this new sample and tip and in a different STM, we observe the same anisotropic amplitudes of the  $2a_0 \times 2a_0$  CDW peaks along the three  $\Gamma$ -M directions (Fig. 4b,c) indicating that the CDW breaks both rotational and mirror symmetries. Second, comparing  $I_1$  and  $I_3$  (left panel in Fig. 4d) under + 2 T and - 2 T fields, we see an intensity reversal. The sign change in  $I_r$  is also accompanied by a change in the relative length of the Bragg vector  $\mathbf{Q}_r$  (right panel, Fig. 4d). Our data thus not only provide independent confirmation of the CDW intensity reversal in magnetic fields seen previously<sup>7,43</sup>, but also uncovers that the reversal is accompanied by field-induced anisotropic strain.

The ability to manipulate the relative intensities of the CDW peaks with linearly polarized light and magnetic field gives us valuable information on the CDW order parameter such as its relation to time-reversal symmetry. To extract this information, we employ a phenomenological analysis of the experimental results, which relies only on symmetry constraints and not on specific microscopic mechanisms. Specifically, we consider a general flux CDW phase described by a three-component CDW order parameter  $\mathbf{L} = (L_1, L_2, L_3)$  with wave-vectors  $\mathbf{Q}_{L_1} = \left(\frac{1}{2}, 0, \frac{1}{2}\right)$ ,  $\mathbf{Q}_{L_2} = \left(0, \frac{1}{2}, \frac{1}{2}\right)$ , and  $\mathbf{Q}_{L_3} = \left(-\frac{1}{2}, +\frac{1}{2}, \frac{1}{2}\right)$ , corresponding to distortions of the V bonds that increase the size of the unit cell by  $2 \times 2 \times 2$ . We also include in the description of the flux CDW phase a time-reversal symmetry-breaking (TRSB) CDW order parameter  $\Phi = (\Phi_1, \Phi_2, \Phi_3)$  with in-plane wave-vectors  $\mathbf{Q}_{M_1} = \left(\frac{1}{2}, 0, 0\right)$ ,  $\mathbf{Q}_{M_2} = \left(0, \frac{1}{2}, 0\right)$ , and  $\mathbf{Q}_{M_3} = \left(-\frac{1}{2}, +\frac{1}{2}, 0\right)$ , corresponding to V orbital magnetism (“loop currents”). Our STM data gives direct access to the intensities  $I_1$ ,  $I_2$  and  $I_3$  of the CDW peaks at  $\mathbf{Q}_1$ ,  $\mathbf{Q}_2$ , and  $\mathbf{Q}_3$  respectively.

In the absence of electromagnetic fields, X-ray data on RbV<sub>3</sub>Sb<sub>5</sub> reveal an orthorhombic crystal structure, which is symmetric with respect to a vertical mirror<sup>40</sup>. As a result, two of the CDW peaks are expected to have the same magnitude – more concretely,  $I_1 = I_3 \neq I_2$  if the

mirror plane is chosen to include the  $\mathbf{Q}_2$  wave-vector. In terms of the CDW order parameters, this implies  $|L_1| = |L_3| \neq |L_2|$ . The fact that in our STM data  $I_1$  and  $I_3$  are slightly different even in the absence of electromagnetic fields is likely due to small residual strain. As our laser measurements have shown, the CDW in these kagome systems is highly sensitive to lattice strain. Our goal is to elucidate what further constraints are imposed to these CDW order parameters by the response of the CDW intensities on the electromagnetic fields.

Let us consider the light-induced response first. Incident light with polarization  $\mathbf{E}_1$  or  $\mathbf{E}_3$  results in a lattice distortion accompanied by  $I_1 \neq I_3$  (Fig. 4e) such that the mirror plane along  $\mathbf{Q}_2$  is broken. This observation suggests that the system has a non-zero electro-striction tensor element  $\chi_{xyxy}^{\text{es}}$ . Such a tensor element is allowed for any CDW configuration with  $|L_1| = |L_3| \neq |L_2|$ , and as such does not impose additional constraints on the type of CDW order, including on the possible emergence of TRSB. Note that, while symmetry allows a non-zero  $\chi_{xyxy}^{\text{es}}$ , it says nothing about its magnitude. The sizable effect of the 1.2 eV optical pulse on the CDW peaks, which are associated with low-energy zone-corner phonon modes, is indicative of a strong electron-phonon non-linear coupling.

The response of the CDW peaks to the out-of-plane magnetic field  $\mathbf{B}_z$  imposes even more severe constraints on the CDW order parameters  $\mathbf{L}$  and  $\Phi$ . The fact that the relative peak intensities  $I_r$  and the ratio of Bragg vectors  $\mathbf{Q}_r$  switch with the direction of  $\mathbf{B}_z$  implies a non-zero piezo-magnetic tensor element  $\chi_{xyz}^{\text{pm}}$  – or, in other words, that an out-of-plane magnetic field induces an in-plane shear lattice distortion (Fig. 4f). First, this type of piezo-magnetic response necessarily implies that the CDW must break time-reversal symmetry, i.e., that not only  $|L_1| = |L_3| \neq |L_2|$ , but also  $|\Phi_1| = |\Phi_3| \neq |\Phi_2|$ . Moreover, as we show in the group theoretical analysis in Methods, it implies a non-zero  $L_2$ , a vanishing  $\Phi_2$ , so that the system does not have a macroscopic magnetic dipole, and, remarkably, a non-trivial relative phase of  $\pi$  between the non-zero components of the two order parameters,  $\text{sign}(L_1 L_3 \Phi_1 \Phi_3) = -1$ . This relative phase has a simple interpretation in terms of the symmetries of the bond-order pattern, described by  $\mathbf{L}$  alone, and the loop-current pattern, described by  $\Phi$  alone. To illustrate this, consider the simpler case of a single kagome layer. Separately, the triple-Q bond-order pattern and the double-Q loop-current pattern each have an in-plane twofold rotation axis (Extended Data Fig. 6a-c). The key point is that the rotation axes do not match if the aforementioned

relative phase is trivial (Fig. 4g), but match when it is non-trivial (Fig. 4h). It is only in the latter case that the combined flux CDW phase possesses an in-plane twofold rotation axis. This is essential for the piezo-magnetic response observed experimentally in the absence of macroscopic magnetization. Upon application of an out-of-plane magnetic field, the two-fold rotation axis is broken, resulting in a shear strain. We dub this unusual phase where the rotation axes of both the bond-order pattern and the loop-current pattern match a congruent flux CDW phase.

A schematic of the response of the CDW, and the corresponding lattice distortions, to electric and magnetic fields is summarized in Fig. 4e,f and 4i. In the absence of the fields and of residual strain, the peaks at the two CDW wave-vectors are equivalent ( $|L_1| = |L_3|$ ), resulting in the schematic double-well free-energy shown by the red curve in Fig. 4i. The application of light with polarization along a particular direction ( $E_1$  for instance, Fig. 4e) changes the free energy landscape in Fig. 4i by favoring one of the two CDW order parameters. This results in an increase in  $I_1$  and a corresponding decrease in the lattice in this direction. This finite electro-striction response is likely mediated by light-activated phonons and non-linear electron-phonon coupling. Similarly, a magnetic field towards the sample surface (Fig. 4f) decreases the lattice parameter along the direction of the Bragg vector  $Q_{B3}$  resulting in an increase in the CDW intensity at  $Q_3$ . Taken together, via its non-trivial and significant electro-striction and piezo-magnetic responses, the system can switch from one local minimum to the other within the free energy landscape shown in Fig. 4i.

The response of the CDW to electromagnetic fields provides strong constraints on the symmetry of the order parameter. The simplest CDW configuration that satisfies these conditions is the congruent flux phase  $\mathbf{L} = (|L_1|, L_2, |L_1|)$  and  $\Phi = (|\Phi_1|, 0, -|\Phi_1|)$ , which has the *magnetic* space group *Cmmm* (#65.481) and which breaks time reversal symmetry (see group theoretical analysis in Methods). Note that this CDW configuration can also address several other experimental observations. First, it is consistent with one of the non-magnetic space groups (*Cmmm*, #65) that were found to possibly refine the crystal structure of  $\text{RbV}_3\text{Sb}_5$  via X-ray data<sup>40</sup>. Second, it is not only consistent with TRSB seen by  $\mu\text{SR}$  experiments, but it can also reconcile the seemingly contradictory spontaneous Kerr effect results reported in the literature. While a pristine sample would not display a spontaneous Kerr effect for this CDW

configuration, as it does not have a macroscopic magnetic dipole moment, the non-zero piezomagnetic tensor element  $\chi_{xyz}^{\text{pm}}$  implies that unintentional shear strain in the sample would generate an out-of-plane magnetic moment, which in turn would give rise to a spontaneous Kerr effect. Lastly, our laser-STM study paves the way to an in-situ optical manipulation of strain and symmetry breaking in quantum materials.

**Figure 1**

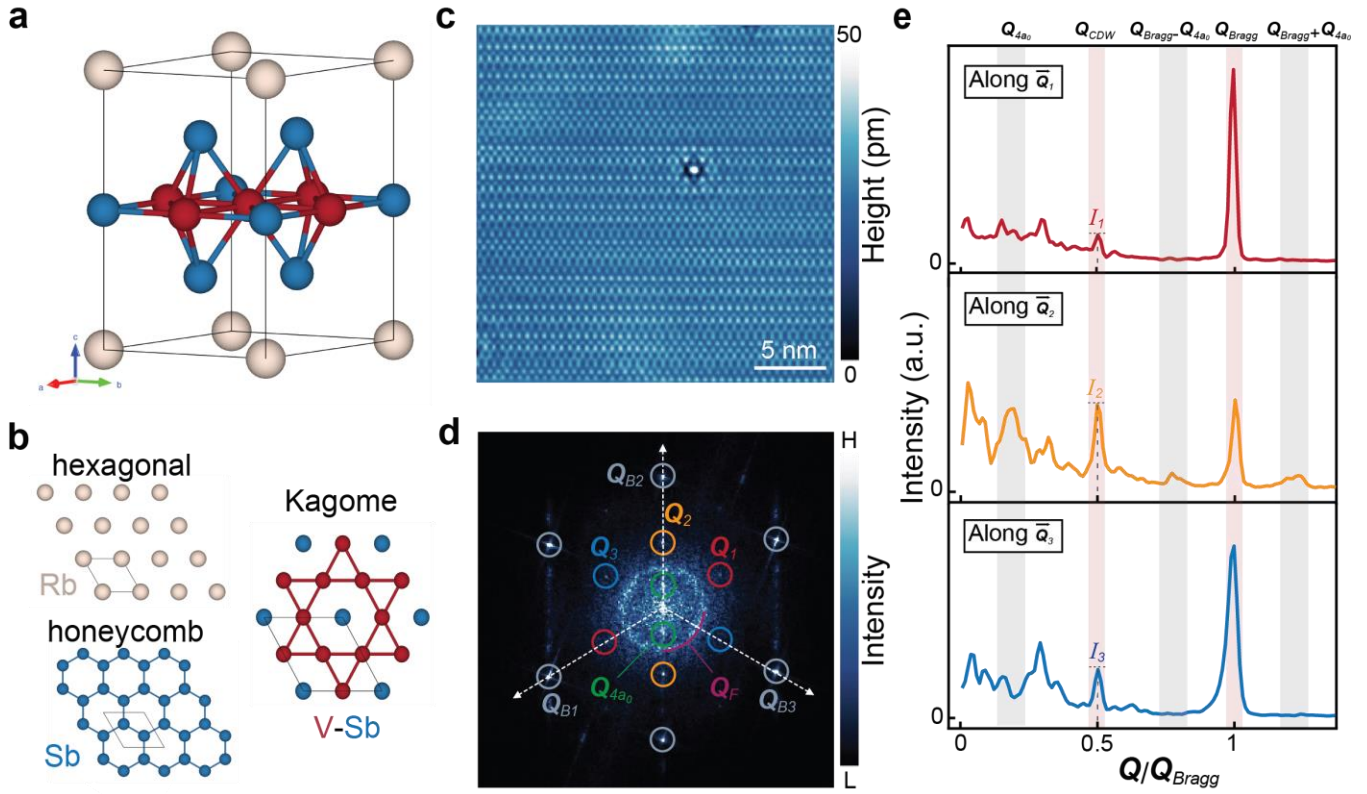


**Fig. 1 | Sb surface identification of  $\text{RbV}_3\text{Sb}_5$  and CDW peak intensities.**

**a**, Atomic structure of  $\text{RbV}_3\text{Sb}_5$ . **b**, Top view of different terminations, showing the hexagonal Rb layer, the honeycomb Sb layer and the kagome V-Sb layer. **c**, Topographic image ( $25 \text{ nm} \times 25 \text{ nm}$ ) of the Sb layer ( $V_{\text{sample}} = -100 \text{ mV}$ ,  $I_{\text{tunneling}} = 175 \text{ pA}$ ). **d**, FT image of the Sb surface, showing the wave vectors  $\mathbf{Q}_{1-3}$  associated with the  $2a_0 \times 2a_0$  CDW,  $\mathbf{Q}_{4a_0}$  associated with unidirectional charge order and  $\mathbf{Q}_F$  associated with isotropic defect scattering related interference patterns. The three Bragg peaks along the  $\Gamma$ -M directions are labelled  $\mathbf{Q}_{B1-B3}$ . **e**, Comparison of linecuts in (d) along the  $\mathbf{Q}_1$  (top),  $\mathbf{Q}_2$  (middle) and  $\mathbf{Q}_3$  (bottom) directions.  $\mathbf{Q}_{4a_0}$  and its satellite Bragg peaks are only prominent along the  $\mathbf{Q}_2$  direction, while the  $2a_0 \times 2a_0$   $\mathbf{Q}_{1-3}$  CDW peaks (labelled on top as  $\mathbf{Q}_{\text{CDW}}$ ) show different intensities in the three directions.

**Figure 2**

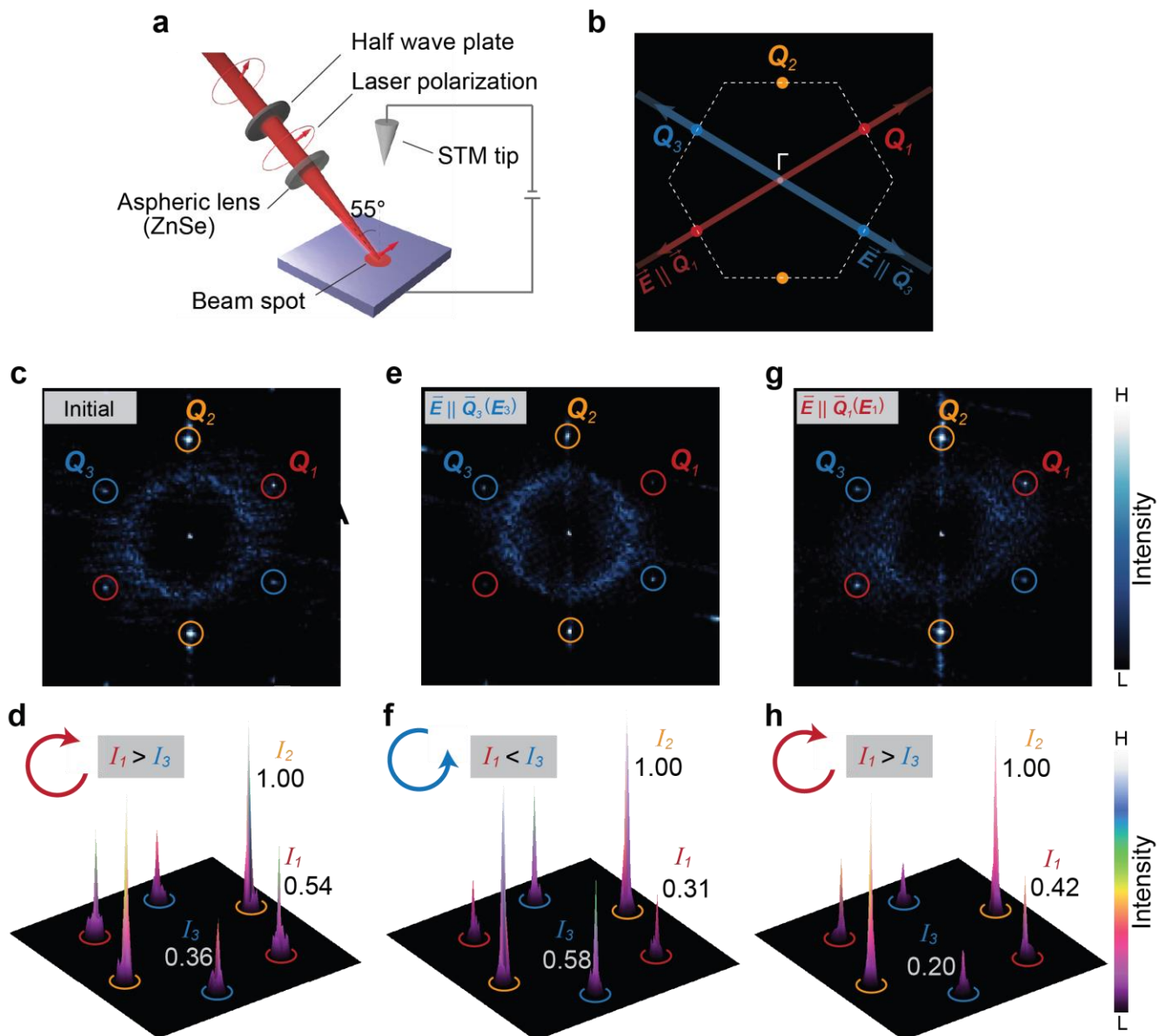


**Fig. 2 | Light-induced switching of the intensity order in  $2a_0 \times 2a_0$  CDW.**

**a**, Schematic illustration of light illumination and subsequent STM measurement on  $\text{RbV}_3\text{Sb}_5$ . **b**, Schematic FT image focusing on the  $2a_0 \times 2a_0$  CDW intensity distribution. The red and blue double arrows denote the polarization direction of the laser beam. **c**, FT of topographic image before light illumination ( $V_s = -100$  mV,  $I_t = 175$  pA). **d**, 3D view of the  $2a_0 \times 2a_0$  CDW intensity peaks of (c), showing  $I_1 > I_3$ , leading to a clockwise order among the relative CDW intensities.

**e**, FT of topographic image of the same region after light illumination with linear polarization parallel to the  $E_3$  direction. **f**, 3D view of (e), showing a reversed CDW intensity order (counterclockwise) compared to (c-d). **g**, FT of topographic image of the same region after light illumination with the linear polarization parallel to  $E_1$ . **h**, 3D view of (g), demonstrating that the intensity order has now switched back to being clockwise.

**Figure 3**

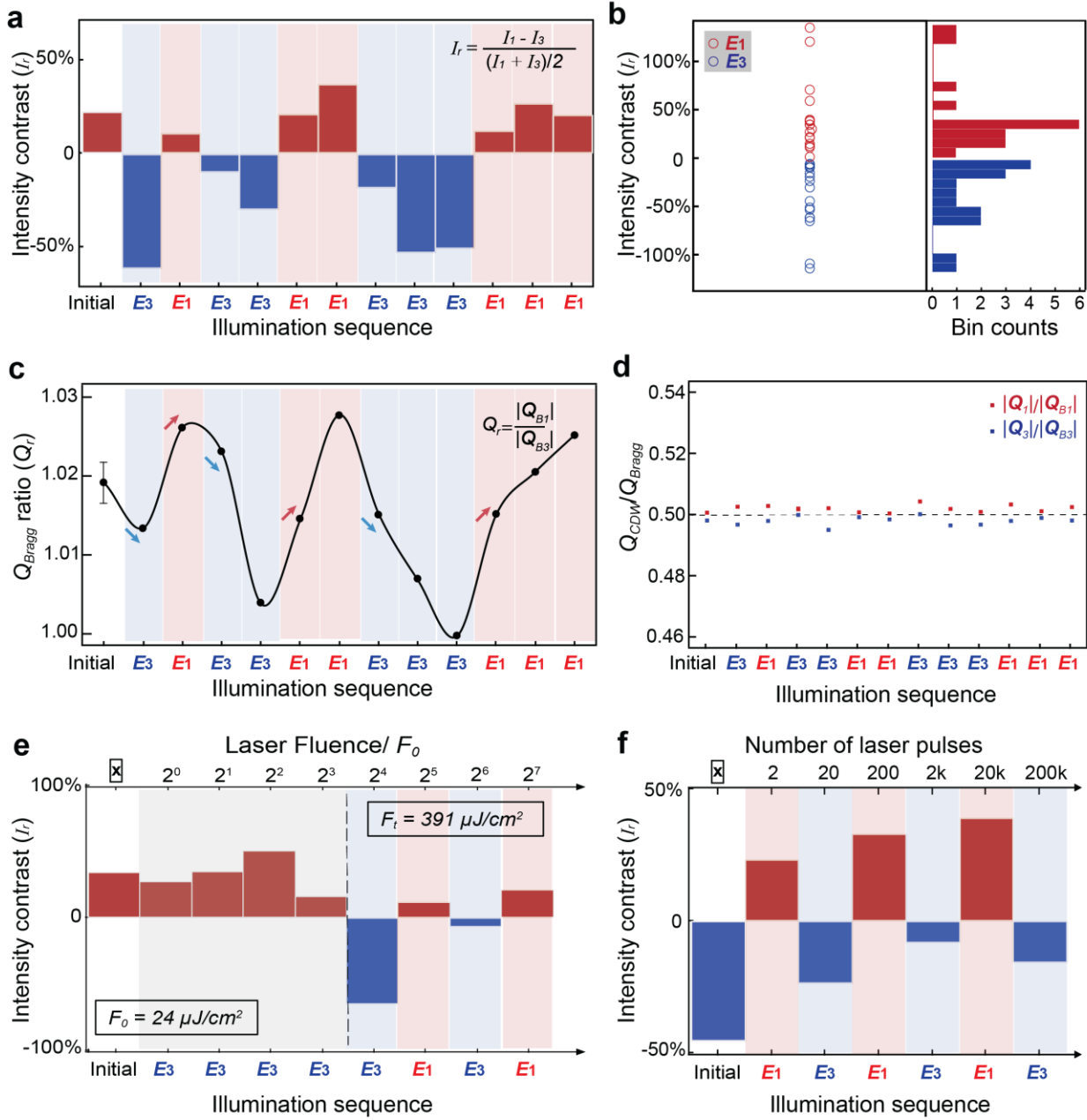


**Fig. 3 | Characterization of the light-induced switching of the relative CDW intensity.**

**a**, Arbitrary illumination sequence with laser polarization along either  $E_1$  or  $E_3$ . The color of the solid bar denotes the sign of the relative intensity ( $I_r$ ) between the  $Q_1$  and  $Q_3$  CDW wave-vectors as defined in the inset. The color of the background indicates the sign of the expected relative CDW intensity order based on the direction of illumination. **b**, Statistics of  $I_r$  for  $E_1$  illuminations (red circles) and  $E_3$  illuminations (blue circles). 34 bin counts in total are displayed

in the left sub-panel. The bin counts for a given intensity contrast range are displayed in the right sub-panel. **c**, Trend of the Bragg peak ratio ( $Q_r$ ) between  $Q_{B1}$  and  $Q_{B3}$  for the arbitrary illumination sequence shown in (a). The error bar represents the full range variation of  $Q_r$  in five sequential measurements of  $Q_r$  with circularly polarized pulsed light, which we have determined does not influence the CDW intensities. **d**,  $Q_{CDW}/Q_{Bragg}$  ratio along  $Q_1$  (red dots) and  $Q_3$  directions (blue dots), showing that the  $2a_0 \times 2a_0$  CDW remains commensurate during the illumination sequence. The dashed line denotes the average  $Q_{CDW}/Q_{Bragg}$  value from all points listed. **e**, Laser pulse fluence dependence of the switching behavior, showing that the threshold fluence to trigger the switching behavior is  $\sim 0.39 \text{ mJ/cm}^2$ . **f**, Dependence of the switching on the number of shots, showing that the CDW intensity order can be switched even with two pulses.

**Figure 4**

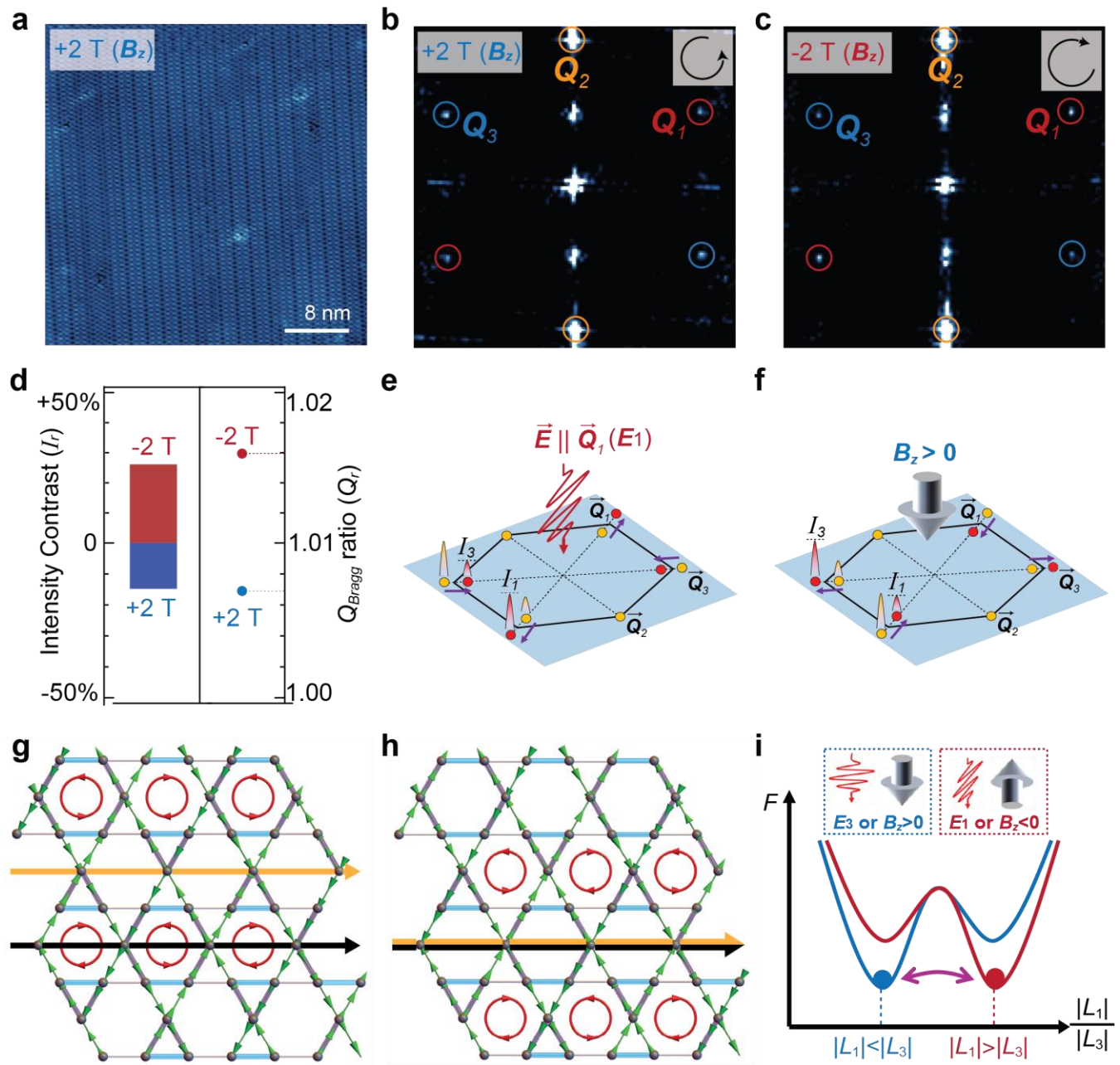


**Fig. 4 | Magnetic-field-induced switching of the relative CDW intensity and the congruent flux-CDW phase.**

**a**, Topographic image of the Sb surface (40 nm x 40 nm) under 2 T magnetic field perpendicular to the sample ( $V_s = -40$  mV,  $I_t = 100$  pA). **b,c**, FT of topography at +2 T/-2 T showing a reversed intensity order between  $Q_1$  and  $Q_3$  depending on the field direction. **d**,

Intensity contrast plot ( $I_r$  in left panel) and Bragg momentum ratio plot ( $Q_r$  in right panel), using the same method as Fig. 3, show that both the CDW intensity order and the lattice distortion along  $Q_1$  and  $Q_3$  can be manipulated by an external magnetic field. **e**, Schematic illustration of the electro-striction response of the system. The wavy line denotes the optical pulse. The wave amplitude direction denotes its polarization direction (here, the  $Q_1$  direction). The position of the red dots and purple arrows represents the response of the Bragg momentum upon illumination. **f**, Schematic illustration of the piezo-magnetic response. The grey 3D arrow denotes the direction of the external magnetic field (here, positive field). **g,h**, An overlayed view of the spatial pattern of Vanadium bond order  $L$  (sky-blue and purple colored bond) and loop current order  $\Phi$  (green arrows). The black/orange lines represent the in-plane 2-fold rotation axes of the bond order/loop current, respectively. The red circle represents the closed current loops. **(g)** For the case when the non-zero components of  $\Phi$  and  $L$  have a trivial relative phase (0),  $L$  and  $\Phi$  do not share the same 2-fold rotation axis. **(h)** For the case when the relative phase is non-trivial ( $\pi$ ),  $L$  and  $\Phi$  share the same rotation axis, resulting in a congruent flux-CDW phase. **i**, Schematic free-energy landscape of the system in terms of the components of the CDW order parameter corresponding to wave-vectors  $Q_1$  and  $Q_3$  under external electromagnetic fields. Note that the curves are schematic and do not necessarily have the same shape for the cases of an applied electric and magnetic field.

## References

1. Haldane, F. D. M. Model for a Quantum Hall Effect without Landau Levels: Condensed-Matter Realization of the ‘Parity Anomaly’. *Phys. Rev. Lett.* **61**, 2015–2018 (1988).
2. Hsu, T. C., Marston, J. B. & Affleck, I. Two observable features of the staggered-flux phase at nonzero doping. *Phys. Rev. B* **43**, 2866–2877 (1991).
3. Varma, C. M. Non-Fermi-liquid states and pairing instability of a general model of copper oxide metals. *Phys. Rev. B* **55**, 14554–14580 (1997).
4. Chakravarty, S., Laughlin, R. B., Morr, D. K. & Nayak, C. Hidden order in the cuprates. *Phys. Rev. B* **63**, 094503 (2001).
5. Ortiz, B. R. *et al.* New kagome prototype materials: discovery of  $\text{KV}_3\text{Sb}_5$ ,  $\text{RbV}_3\text{Sb}_5$ , and  $\text{CsV}_3\text{Sb}_5$ . *Phys. Rev. Mater.* **3**, 094407 (2019).
6. Ortiz, B. R. *et al.*  $\text{CsV}_3\text{Sb}_5$ : A  $Z_2$  Topological Kagome Metal with a Superconducting Ground State. *Phys. Rev. Lett.* **125**, 247002 (2020).
7. Jiang, Y.-X. *et al.* Unconventional chiral charge order in kagome superconductor  $\text{KV}_3\text{Sb}_5$ . *Nat. Mater.* **20**, 1353–1357 (2021).
8. Yu, L. *et al.* Evidence of a hidden flux phase in the topological kagome metal  $\text{CsV}_3\text{Sb}_5$ . Preprint at <https://doi.org/10.48550/arXiv.2107.10714> (2021).
9. Mielke, C. *et al.* Time-reversal symmetry-breaking charge order in a kagome superconductor. *Nature* **602**, 245–250 (2022).
10. Khasanov, R. *et al.* Time-reversal symmetry broken by charge order in  $\text{CsV}_3\text{Sb}_5$ . *Phys. Rev. Res.* **4**, 023244 (2022).
11. Xu, Y. *et al.* Three-state nematicity and magneto-optical Kerr effect in the charge density waves in kagome superconductors. *Nat. Phys.* **18**, 1470–1475 (2022).
12. Wu, Q. *et al.* Simultaneous formation of two-fold rotation symmetry with charge order in the kagome superconductor  $\text{CsV}_3\text{Sb}_5$  by optical polarization rotation measurement. *Phys. Rev. B* **106**, 205109 (2022).
13. Guo, C. *et al.* Switchable chiral transport in charge-ordered kagome metal  $\text{CsV}_3\text{Sb}_5$ . *Nature* **611**, 461–466 (2022).
14. Hu, Y. *et al.* Time-reversal symmetry breaking in charge density wave of  $\text{CsV}_3\text{Sb}_5$  detected by polar Kerr effect. Preprint at <https://doi.org/10.48550/arXiv.2208.08036> (2023).
15. Li, H. *et al.* Rotation symmetry breaking in the normal state of a kagome superconductor  $\text{KV}_3\text{Sb}_5$ . *Nat. Phys.* **18**, 265–270 (2022).
16. Saykin, D. R. *et al.* High Resolution Polar Kerr Effect Studies of  $\text{CsV}_3\text{Sb}_5$ : Tests for Time Reversal Symmetry Breaking Below the Charge Order Transition. Preprint at <https://doi.org/10.48550/arXiv.2209.10570> (2022).
17. Farhang, C., Wang, J., Ortiz, B. R., Wilson, S. D. & Xia, J. Unconventional Optical Rotation in the Charge Ordered State of Kagome Metal  $\text{CsV}_3\text{Sb}_5$ . Preprint at <https://doi.org/10.48550/arXiv.2303.10265> (2023).

18. Guo, H.-M. & Franz, M. Topological insulator on the kagome lattice. *Phys. Rev. B* **80**, 113102 (2009).
19. Tang, E., Mei, J.-W. & Wen, X.-G. High-Temperature Fractional Quantum Hall States. *Phys. Rev. Lett.* **106**, 236802 (2011).
20. Kiesel, M. L., Platt, C. & Thomale, R. Unconventional Fermi Surface Instabilities in the Kagome Hubbard Model. *Phys. Rev. Lett.* **110**, 126405 (2013).
21. Chen, H., Niu, Q. & MacDonald, A. H. Anomalous Hall Effect Arising from Noncollinear Antiferromagnetism. *Phys. Rev. Lett.* **112**, 017205 (2014).
22. Ye, L. *et al.* Massive Dirac fermions in a ferromagnetic kagome metal. *Nature* **555**, 638–642 (2018).
23. Yin, J.-X. *et al.* Giant and anisotropic many-body spin–orbit tunability in a strongly correlated kagome magnet. *Nature* **562**, 91–95 (2018).
24. Lin, Z. *et al.* Flatbands and Emergent Ferromagnetic Ordering in  $\text{Fe}_3\text{Sn}_2$  Kagome Lattices. *Phys. Rev. Lett.* **121**, 096401 (2018).
25. Morali, N. *et al.* Fermi-arc diversity on surface terminations of the magnetic Weyl semimetal  $\text{Co}_3\text{Sn}_2\text{S}_2$ . *Science* **365**, 1286–1291 (2019).
26. Liu, D. F. *et al.* Magnetic Weyl semimetal phase in a Kagomé crystal. *Science* **365**, 1282–1285 (2019).
27. Yin, J.-X. *et al.* Quantum-limit Chern topological magnetism in  $\text{TbMn}_6\text{Sn}_6$ . *Nature* **583**, 533–536 (2020).
28. Teng, X. *et al.* Discovery of charge density wave in a kagome lattice antiferromagnet. *Nature* **609**, 490–495 (2022).
29. Oey, Y. M. *et al.* Fermi level tuning and double-dome superconductivity in the kagome metal  $\text{CsV}_3\text{Sb}_{5-x}\text{Sn}_x$ . *Phys. Rev. Materials* **6**, L041801 (2022).
30. Zheng, L. *et al.* Emergent charge order in pressurized kagome superconductor  $\text{CsV}_3\text{Sb}_5$ . *Nature* **611**, 682–687 (2022).
31. Zhong, Y. *et al.* Nodeless electron pairing in  $\text{CsV}_3\text{Sb}_5$ -derived kagome superconductors. *Nature* **617**, 488–492 (2023).
32. Zhu, C. C. *et al.* Double-dome superconductivity under pressure in the V-based kagome metals  $\text{AV}_3\text{Sb}_5$  (A=Rb and K). *Phys. Rev. B* **105**, 094507 (2022).
33. Feng, X., Jiang, K., Wang, Z. & Hu, J. Chiral flux phase in the Kagome superconductor  $\text{AV}_3\text{Sb}_5$ . *Science Bulletin* **66**, 1384–1388 (2021).
34. Denner, M. M., Thomale, R. & Neupert, T. Analysis of Charge Order in the Kagome Metal  $\text{AV}_3\text{Sb}_5$  (A = K, Rb, Cs). *Phys. Rev. Lett.* **127**, 217601 (2021).
35. Park, T., Ye, M. & Balents, L. Electronic instabilities of kagome metals: Saddle points and Landau theory. *Phys. Rev. B* **104**, 035142 (2021).
36. Lin, Y.-P. & Nandkishore, R. M. Complex charge density waves at Van Hove singularity on hexagonal lattices: Haldane-model phase diagram and potential realization in the kagome metals  $\text{AV}_3\text{Sb}_5$  (A=K, Rb, Cs). *Phys. Rev. B* **104**, 045122 (2021).

37. Zhou, S. & Wang, Z. Chern Fermi pocket, topological pair density wave, and charge-4e and charge-6e superconductivity in kagomé superconductors. *Nat. Commun.* **13**, 7288 (2022).
38. Christensen, M. H., Birol, T., Andersen, B. M. & Fernandes, R. M. Loop currents in  $AV_3Sb_5$  kagomé metals: Multipolar and toroidal magnetic orders. *Phys. Rev. B* **106**, 144504 (2022).
39. Stahl, Q. *et al.* Temperature-driven reorganization of electronic order in  $CsV_3Sb_5$ . *Phys. Rev. B* **105**, 195136 (2022).
40. Kautzsch, L. *et al.* Structural evolution of the kagomé superconductors  $AV_3Sb_5$  (A = K, Rb, and Cs) through charge density wave order. *Phys. Rev. Mater.* **7**, 024806 (2023).
41. Xiao, Q. *et al.* Coexistence of multiple stacking charge density waves in kagomé superconductor  $CsV_3Sb_5$ . *Phys. Rev. Res.* **5**, L012032 (2023).
42. Zhao, H. *et al.* Cascade of correlated electron states in the kagomé superconductor  $CsV_3Sb_5$ . *Nature* **599**, 216–221 (2021).
43. Shumiya, N. *et al.* Intrinsic nature of chiral charge order in the kagomé superconductor  $RbV_3Sb_5$ . *Phys. Rev. B* **104**, 035131 (2021).
44. Yu, J. *et al.* Evolution of Electronic Structure in Pristine and Rb-Reconstructed Surfaces of Kagome Metal  $RbV_3Sb_5$ . *Nano Lett.* **22**, 918–925 (2022).
45. Chen, H. *et al.* Roton pair density wave in a strong-coupling kagomé superconductor. *Nature* **599**, 222–228 (2021).
46. Li, H. *et al.* Unidirectional coherent quasiparticles in the high-temperature rotational symmetry broken phase of  $AV_3Sb_5$  kagomé superconductors. *Nat. Phys.* **19**, 637–643 (2023).
47. Christensen, M. H., Birol, T., Andersen, B. M. & Fernandes, R. M. Theory of the charge-density wave in  $AV_3Sb_5$  kagomé metals. *Phys. Rev. B* **104**, 214513 (2021).

## **Acknowledgements**

The laser-STM studies were supported by the Gordon and Betty Moore Foundation's EPiQS initiative through Grant No. GBMF9465. This material is based upon work supported by the U.S. Department of Energy Office of Science National Quantum Information Science Research Centers as part of the Q-NEXT center, which supported the work of S. B. and V. M and provided partial support for laser-STM development. Funding for sample growth was provided via the UC Santa Barbara NSF Quantum Foundry funded via the Q-AMASE-i program under award DMR-1906325. A.C.S. acknowledges support from the Eddleman Center for Quantum Innovation at UC Santa Barbara. E.R, F.Y. and T.B. were supported by the NSF CAREER grant DMR-2046020. R.M.F. was supported by the Air Force Office of Scientific Research under Award No. FA9550-21-1-0423. Z. W. is supported by the U.S. Department of Energy, Basic Energy Sciences (Grant No. DE-FG02-99ER45747) and by Research Corporation for Science Advancement (Cottrell SEED Award No. 27856).

## **Author Contributions:**

Y. X., S. B., V. M. conceived the project. Y.X. and S.B. conducted laser-STM measurement. S. B. designed and constructed the laser-STM setup. Y.X. conducted STM study under magnetic field. A.C.S, B.R.O. and S.D.W. provided  $\text{RbV}_3\text{Sb}_5$  samples used in this study. E.R, F.W., T. B., Z.W., and R. M. F. conducted group theory analysis and theoretical interpretation of the data. Y.X., S.B., and V. M. performed data analysis and wrote the manuscript with input from all the authors.

**Competing interests:** The authors declare that they have no competing interests.

**Data Availability:** All of the data for the main figures will be uploaded to the Illinois Databank.

# Methods and Extended Data Figures for

## Optical Manipulation of the Charge Density Wave state in $\text{RbV}_3\text{Sb}_5$

### Table of Contents

#### **Methods**

- 1: Single crystal growth of  $\text{RbV}_3\text{Sb}_5$
- 2: Scanning tunneling microscopy/spectroscopy
- 3: Laser parameters, optics setup, and experimental procedure for laser-STM
- 4: Group theoretical analysis on the response of CDW order parameter under electric and magnetic field

#### **Extended Data Table 1:**

Magnetic space groups for different combinations of the bond-order CDW and the loop-current CDW order parameters.

#### **Extended Data Figure 1-6:**

- 1: Revealing Sb surface atomically precise sweeping method.
- 2: High-resolution topography and lattice constant of Sb layer.
- 3: Optics layout of the laser-STM setup.
- 4: Identification of Bragg peak vector locations.
- 5: Trend of CDW peak vector ratio between  $Q_1$  and  $Q_3$  for an arbitrary laser illumination sequence.
- 6: Vanadium bond order and loop current pattern and their rotation axis for different order parameter configurations.

#### Single crystal growth of $\text{RbV}_3\text{Sb}_5$

Single crystals of  $\text{RbV}_3\text{Sb}_5$  were synthesized from Rb (ingot, Alfa 99.75%), V (powder, Sigma 99.9%, purified in an HCl and Ethanol mixture), and Sb (shot, Alfa 99.999%) using a modified self-flux method. Inside an argon glovebox with oxygen and moisture levels  $< 0.5$  ppm, elemental reagents were weighed out to composition  $\text{Rb}_{20}\text{V}_{15}\text{Sb}_{120}$ , and loaded into a tungsten carbide vial to be milled for 60 min in a SPEX 8000D mill. Resulting powder was loaded into 2 mL alumina (Coorstek) crucibles and sealed inside steel tubes under argon. Sample was heated to 1000 °C at 200 °C/hour, soaked at that temperature for 12 hours, then cooled down to 900 °C at 5 °C, to finally be slow-cooled to 500 °C at a rate of 1°C /hour. Single crystals of

RbV<sub>3</sub>Sb<sub>5</sub> were obtained and mechanically extracted, with typical dimensions of 2 mm x 2 mm x 200  $\mu$ m.

### **Scanning tunneling microscopy/spectroscopy**

The RbV<sub>3</sub>Sb<sub>5</sub> samples used in the experiments cleaved *in situ* at ~90 K and immediately transferred to an STM chamber. All STM experiments were performed in an ultrahigh vacuum ( $1 \times 10^{-10}$  mbar). Laser-coupled STM measurements were conducted under 4 K and Perpendicular magnetic field coupled STM measurements were studied under 1.7 K. All the scanning parameter (setpoint voltage and current) of the STM topographic images are listed in the captions of the figures. Unless otherwise noted, the differential conductance (dI/dV) spectra were acquired by a standard lock-in amplifier at a modulation frequency of 913.1 Hz. STM tip made from tungsten was fabricated via electrochemical etching.

### **Laser parameters, optics setup, and experimental procedure for laser-STM**

The optical excitation used in this experiment is given by  $2 \times 10^5$  burst shots of laser pulse train at 100 kHz repetition rate and at 0.39 mJ/cm<sup>2</sup> fluence (otherwise mentioned), 1025 nm wavelength (1.21 eV), and 250 fs pulse width. The laser beam is generated by Yb:KGW RA laser system (PHAROS PH2-10W, Light Conversion). The pulse train timing is controlled by an arbitrary function generator (ARB Rider 2182, Active Technologies) which directly triggers a pulse picker inside the RA laser system. As seen from the detailed layout of the laser-STM setup in Extended Data Fig. 3. The beam passes through a half-wave plate for the polarization direction control. The half-wave plate rotates the polarization to a direction of interest. Then the beam is guided to the tip-sample junction area inside the USM1200LL STM (Unisoku) through a CaF<sub>2</sub> viewport (MPF) and ZnSe aspheric lens (Avantier Inc.) which acts as an objective lens. The focal length of the ZnSe lens at 1025 nm is 12.43 mm. The alignment of the beam spot and the STM tip-sample junction is monitored by an optical microscope setting which consists of another ZnSe lens, N-BK7 plano-convex lens, and a CMOS camera. During the alignment check, the laser beam is switched to continuous pulse train mode and pass through an OD > 2.0 ND filter to prevent melting of the sample surface. The alignment is adjusted by moving the

lens piezo stages where ZnSe lenses are mounted. The incident angle of the beam to the surface normal direction of the sample is 55 degrees. The beam is focused to an elliptic spot (due to the incidence angle) with a size estimated to be  $49 \mu\text{m} \times 68 \mu\text{m}$  ( $1/e^2$  diameter). When the actual burst shots are illuminated to the sample, the tip is retracted to the surface normal direction by  $\approx 70 \mu\text{m}$  in order to prevent any damage or change to the tip during illumination. After the burst illumination, the tip is reapproached with a shift in the lateral position typically less than 10 nm so that one can easily locate the cleaned Sb surface area under study again.

### **Group theoretical analysis on the response of CDW order parameter under electric and magnetic field**

Our starting point to interpret the STM data is a “real” CDW order parameter  $\mathbf{L} = (L_1, L_2, L_3)$ , corresponding to in-plane and out-of-plane distortions of the V-V bonds, and an “imaginary” CDW order parameter  $\Phi = (\Phi_1, \Phi_2, \Phi_3)$ , which corresponds to in-plane orbital magnetic currents involving the V states. In terms of the  $P6/mmm$  space group (#191) of  $\text{AV}_3\text{Sb}_5$ ,  $\mathbf{L}$  transforms as the  $L_2^-$  irreducible representation (irrep). Thus, each component  $L_i$  is associated with each wave-vector  $\mathbf{Q}_{L_1} = \left(\frac{1}{2}, 0, \frac{1}{2}\right)$ ,  $\mathbf{Q}_{L_2} = \left(0, \frac{1}{2}, \frac{1}{2}\right)$ , and  $\mathbf{Q}_{L_3} = \left(-\frac{1}{2}, +\frac{1}{2}, \frac{1}{2}\right)$ , respectively; note that the three different  $\mathbf{Q}_{L_i}$  are related by a threefold rotation. On the other hand,  $\Phi$  transforms as the  $mM_2^+$  irrep (where  $m$  indicates that it is odd under time reversal) and thus each component  $\Phi_i$  has wave-vector  $\mathbf{Q}_{M_1} = \left(\frac{1}{2}, 0, 0\right)$ ,  $\mathbf{Q}_{M_2} = \left(0, \frac{1}{2}, 0\right)$ , and  $\mathbf{Q}_{M_3} = \left(-\frac{1}{2}, +\frac{1}{2}, 0\right)$ . Note that  $mM_2^+$  is the simplest type of loop-current order that can be constructed out of the low-energy van Hove singularities (vHs), corresponding to intra-orbital (or intra-vHs) order<sup>1</sup>. Because in DFT both the phonon mode  $L_2^-$  and the phonon mode  $M_1^+$  irrep are unstable, we also consider the real CDW order parameter  $\mathbf{M} = (M_1, M_2, M_3)$  for completeness<sup>2</sup>. Note that  $\mathbf{M}$  transforms as the  $M_1^+$  irrep and, like  $\Phi$ , also has wave-vector  $\mathbf{Q}_{M_1} = \left(\frac{1}{2}, 0, 0\right)$ ,  $\mathbf{Q}_{M_2} = \left(0, \frac{1}{2}, 0\right)$ , and  $\mathbf{Q}_{M_3} = \left(-\frac{1}{2}, +\frac{1}{2}, 0\right)$ . In the notation adopted here, the reciprocal lattice vectors are given by:

$$\mathbf{G}_1 = \frac{2\pi}{a} \left(1, \frac{1}{\sqrt{3}}, 0\right)$$

$$\begin{aligned}
\mathbf{G}_2 &= \frac{2\pi}{a} \left( 0, \frac{2}{\sqrt{3}}, 0 \right) \\
\mathbf{G}_3 &= \frac{2\pi}{c} (0, 0, 1)
\end{aligned} \tag{1}$$

We start by writing down the full Landau free-energy for the coupled order parameters,  $F = F_L + F_\Phi + F_M + F_{L\Phi} + F_{LM} + F_{\Phi M}$ . We have, for the free terms (see also Ref. <sup>1</sup>):

$$\begin{aligned}
F_L &= \frac{a_L}{2} \sum_i L_i^2 + \frac{u_L}{4} \left( \sum_i L_i^2 \right)^2 + \frac{\lambda_L}{4} (L_1^2 L_2^2 + L_1^2 L_3^2 + L_2^2 L_3^2) \\
F_\Phi &= \frac{a_\Phi}{2} \sum_i \Phi_i^2 + \frac{u_\Phi}{4} \left( \sum_i \Phi_i^2 \right)^2 + \frac{\lambda_\Phi}{4} (\Phi_1^2 \Phi_2^2 + \Phi_1^2 \Phi_3^2 + \Phi_2^2 \Phi_3^2) \\
F_M &= \frac{a_M}{2} \sum_i M_i^2 + \frac{\gamma_M}{3} M_1 M_2 M_3 + \frac{u_M}{4} \left( \sum_i M_i^2 \right)^2 + \frac{\lambda_M}{4} (M_1^2 M_2^2 + M_1^2 M_3^2 + M_2^2 M_3^2)
\end{aligned} \tag{2}$$

For the coupled terms, we obtain:

$$\begin{aligned}
F_{L\Phi} &= \frac{\kappa_{L\Phi}}{4} (L_1 L_2 \Phi_1 \Phi_2 + L_1 L_3 \Phi_1 \Phi_3 + L_2 L_3 \Phi_2 \Phi_3) \\
&+ \frac{\lambda_{L\Phi}}{4} (L_1^2 \Phi_1^2 + L_2^2 \Phi_2^2 + L_3^2 \Phi_3^2) + \frac{u_{L\Phi}}{4} \left( \sum_i L_i^2 \right) \left( \sum_i \Phi_i^2 \right)
\end{aligned} \tag{3}$$

as well as

$$\begin{aligned}
F_{LM} &= \frac{\gamma_{LM}}{3} (L_1 L_2 M_3 + L_1 L_3 M_2 + L_2 L_3 M_1) + \frac{\kappa_{LM}}{4} (M_1 M_2 L_1 L_2 + M_1 M_3 L_1 L_3 + M_2 M_3 L_2 L_3) \\
&+ \frac{\lambda_{LM}}{4} (M_1^2 L_1^2 + M_2^2 L_2^2 + M_3^2 L_3^2) + \frac{u_{LM}}{4} \left( \sum_i M_i^2 \right) \left( \sum_i L_i^2 \right)
\end{aligned} \tag{4}$$

and

$$F_{\Phi M} = \frac{\gamma_{\Phi M}}{3} (\Phi_1 \Phi_2 M_3 + \Phi_1 \Phi_3 M_2 + \Phi_2 \Phi_3 M_1) + \frac{\kappa_{\Phi M}}{4} (M_1 M_2 \Phi_1 \Phi_2 + M_1 M_3 \Phi_1 \Phi_3 + M_2 M_3 \Phi_2 \Phi_3)$$

$$+ \frac{\lambda_{\Phi M}}{4} (M_1^2 \Phi_1^2 + M_2^2 \Phi_2^2 + M_3^2 \Phi_3^2) + \frac{u_{\Phi M}}{4} \left( \sum_i M_i^2 \right) \left( \sum_i \Phi_i^2 \right) \quad (5)$$

Rather than minimizing the free energy, we look for order parameter configurations that can explain the STM data. For concreteness, we will consider the instabilities driven by the **L** and **Φ** channels, such that the accompanying **M** order parameter follows trivially from the trilinear couplings  $\gamma_{LM}$ ,  $\gamma_{\Phi M}$  above.

The key quantity measured by STM is the relative intensity between the three CDW peaks at wave-vectors  $\mathbf{Q}_{M_1} = (1/2, 0, 0)$ ,  $\mathbf{Q}_{M_2} = (0, 1/2, 0)$ , and  $\mathbf{Q}_{M_3} = (-1/2, +1/2, 0)$  which correspond to  $\mathbf{Q}_1$ ,  $\mathbf{Q}_2$ , and  $\mathbf{Q}_3$  in the main text. It can be conveniently described in terms of the following two-component “vector” (see, e.g. Ref. <sup>2</sup>):

$$\psi_M = \begin{pmatrix} M_1^2 + M_3^2 - 2M_2^2 \\ \sqrt{3}(M_3^2 - M_1^2) \end{pmatrix} \quad (6)$$

which transforms as the  $\Gamma_5^+$  irrep. Indeed, if all three peaks have the same intensity,  $M_1^2 = M_2^2 = M_3^2$ ,  $\psi_M \sim (0 \ 0)^T$ . On the other hand, if one of the peaks is stronger or weaker than the other two, say  $M_2^2 \neq M_1^2 = M_3^2$ , then  $\psi_M \sim (1 \ 0)^T$ . The other two possibilities, corresponding to  $M_1^2 \neq M_2^2 = M_3^2$  and  $M_3^2 \neq M_1^2 = M_2^2$ , give  $\psi_M \sim (1 \ \sqrt{3})^T$  and  $\psi_M \sim (1 \ -\sqrt{3})^T$ . Any other non-zero value of  $\psi_M$  corresponds to three different peak intensities. Importantly, the quantity  $\psi_M$  has the same transformation properties as:

$$\psi_L = \begin{pmatrix} L_1^2 + L_3^2 - 2L_2^2 \\ \sqrt{3}(L_3^2 - L_1^2) \end{pmatrix} \quad (7)$$

Therefore, hereafter, we will focus only on  $\psi_L$ . The three values associated with the case where one peak is stronger or weaker than the other two equivalent peaks correspond to:

$$\psi_L^1 \sim \begin{pmatrix} 1 \\ 0 \end{pmatrix}, \quad \psi_L^2 \sim \begin{pmatrix} 1 \\ \sqrt{3} \end{pmatrix}, \quad \psi_L^3 \sim \begin{pmatrix} 1 \\ -\sqrt{3} \end{pmatrix} \quad (8)$$

Clearly,  $\psi_L^1$ ,  $\psi_L^2$ , and  $\psi_L^3$ , are related by a  $120^\circ$  rotation. Therefore, if one peak becomes different than the other two, three-fold rotational symmetry is broken. Note, however, that there

remains a vertical mirror plane – or, equivalently, an in-plane two-fold rotation axis  $C'_2$ . These results can also be obtained by noticing that the in-plane strain components  $\varepsilon_{xx} - \varepsilon_{yy}$  and  $\varepsilon_{xy}$  also transform as the same  $\Gamma_5^+$  irrep as  $\psi_M$  and  $\psi_L$ :

$$\varepsilon_{\parallel} = \begin{pmatrix} \varepsilon_{xx} - \varepsilon_{yy} \\ -2\varepsilon_{xy} \end{pmatrix} \quad (9)$$

where  $\varepsilon_{ij} \equiv (\partial_i u_j + \partial_j u_i)/2$  and  $u$  is the displacement vector. The coupling to the  $L$  order parameter is given by:

$$F_{L\varepsilon} = \alpha_1 [(\varepsilon_{xx} - \varepsilon_{yy})(L_1^2 + L_3^2 - 2L_2^2) - 2\sqrt{3}\varepsilon_{xy}(L_3^2 - L_1^2)] \quad (10)$$

where  $\alpha_1$  is some coupling constant. Hence, if  $\psi_L$  is in one of the three configurations described by Eq. (8), the system is in an orthorhombic phase, whereas for any other non-zero  $\psi_L$  values, the system is in a monoclinic phase.

We start by analyzing the STM results in the absence of electromagnetic fields. Previous x-ray measurements have shown that the system is in an orthorhombic phase<sup>3</sup>. For concreteness, we choose the configuration corresponding to  $\psi_L^1$ , i.e.  $|L_1| = |L_3| \neq L_2$ . From Eq. (10), we see that while  $\varepsilon_{xx} \neq \varepsilon_{yy}$ , there is no shear strain,  $\varepsilon_{xy} = 0$ . Moreover, in this case, the vertical mirror plane contains the reciprocal lattice vectors  $\mathbf{G}_2$  and  $\mathbf{G}_3$  and is thus perpendicular to the  $\hat{q}_x$  axis in momentum space,  $\hat{q}_x \equiv (1, -1/2, 0)$ . We note that, in the experiments, the CDW peaks corresponding to  $L_1$  and  $L_3$  are slightly different. We attribute this behavior to residual shear strain  $\varepsilon_{xy}$  present in the sample which, via the coupling in Eq. (10), induces  $L_3^2 \neq L_1^2$ .

Consider now the application of an in-plane electric field  $E_{\parallel} = (E_x, E_y)$ . Since it transforms as the  $\Gamma_6^-$  irrep, its coupling to the  $L$  order parameter has a similar form as Eq. (10):

$$F_{LE} = \alpha_2 [(E_x^2 - E_y^2)(L_1^2 + L_3^2 - 2L_2^2) - 2\sqrt{3}E_x E_y(L_3^2 - L_1^2)] \quad (11)$$

Parametrizing  $E_{\parallel} = E_0(\cos \theta, \sin \theta)$ , we have:

$$F_{LE} = \alpha_2 E_0^2 [\cos 2\theta(L_1^2 + L_3^2 - 2L_2^2) - \sqrt{3} \sin 2\theta(L_3^2 - L_1^2)] \quad (12)$$

In the experiments, the electric field is applied either along the  $Q_{M_1} \equiv (1/2, 0, 0) = \frac{\pi}{a} (1, \frac{1}{\sqrt{3}}, 0)$  direction or the  $Q_{M_3} \equiv (-1/2, +1/2, 0) = \frac{\pi}{a} (-1, \frac{1}{\sqrt{3}}, 0)$  direction. In terms of their polar angles  $\theta_1$  and  $\theta_3$ , these two directions are related according to  $\theta_3 = \pi - \theta_1$ . As a result,  $\cos 2\theta_1 = \cos 2\theta_3$  but  $\sin 2\theta_1 = -\sin 2\theta_3$ . Consequently, according to Eq. (12), application of an electric field along these two directions leads to a splitting of the two CDW peaks,  $L_3^2 - L_1^2 = \pm \delta L^2$ , with opposite signs for a field along  $\theta_1$  and a field along  $\theta_3$ . In terms of the strain tensor, the coupling in Eq. (12) can be written as:

$$F_{\epsilon E} = \alpha'_2 [(E_x^2 - E_y^2)(\epsilon_{xx} - \epsilon_{yy}) + 4E_x E_y \epsilon_{xy}] \quad (13)$$

From the definition of the electro-striction response tensor,  $\epsilon_{ij} = \gamma_{ijkl} E_j E_k$ , we readily identify  $\alpha'_2 \propto \gamma_{66}$  (in Voigt notation) or, using the main text notation for  $\gamma_{ijkl}$ ,  $\alpha'_2 \propto \chi_{xyxy}^{\text{es}}$ . This tensor element is allowed (i.e. not enforced to be zero by symmetry) for both orthorhombic groups *Fmmm* and *Cmmm*, as well as for the hexagonal group *P6/mmm*. Therefore, the STM observation of a switch in the relative intensity of the CDW peaks at  $Q_{M_1}$  and  $Q_{M_3}$  when the electric field direction is switched between the two directions does not require that the CDW breaks time-reversal symmetry.

Consider now the application of an out-of-plane magnetic field  $B_z$ , which transforms as the  $m\Gamma_2^+$  irrep. The STM data shows that the CDW peaks  $L_1^2$  and  $L_3^2$  become different, and that the relative intensity flips sign when  $B_z$  changes sign. According to Eq. (10), a difference in  $L_1^2$  and  $L_3^2$  triggers a shear distortion  $\epsilon_{xy} \neq 0$ , whose sign depends on the sign of the magnetic field. Now, the piezomagnetic response tensor is defined as  $\epsilon_{ij} = \Lambda_{ijk} B_k$ . Hence, this observation implies a non-zero tensor element  $\Lambda_{63} \neq 0$  (in mixed Voigt notation) or, using the notation of the main text for  $\Lambda_{ijk}$ , a non-zero  $\chi_{xyz}^{\text{pm}}$ .

Clearly,  $\Lambda_{63} \neq 0$  requires that time-reversal symmetry is broken, which suggests that the CDW phase must contain a non-zero orbital magnetic density-wave order parameter  $\Phi$ . To identify under which configurations of  $\mathbf{L}$  and  $\Phi$  a non-zero  $\Lambda_{63}$  is allowed, we write down their coupling to  $B_z$  and  $\epsilon_{\parallel}$  (to leading order):

$$F_{L\Phi,B\varepsilon} = \alpha_3 B_z \left[ \sqrt{3} \varepsilon_{xy} L_2 (\Phi_1 L_3 - \Phi_3 L_1) - \frac{1}{2} (\varepsilon_{xx} - \varepsilon_{yy}) (\Phi_1 L_2 L_3 - 2\Phi_2 L_1 L_3 + \Phi_3 L_1 L_2) \right] \quad (14)$$

We can readily identify:

$$\Lambda_{63} = \alpha_3 \sqrt{3} L_2 (\Phi_1 L_3 - \Phi_3 L_1) \quad (15)$$

Recall that the constraints on  $\mathbf{L}$  so far are  $|L_1| = |L_3| \neq L_2$ . A non-zero  $\Lambda_{63}$  further requires  $|\Phi_1| = |\Phi_3|$  and  $\text{sign}(L_1 L_3 \Phi_1 \Phi_3) = -1$ , i.e. it imposes constraints not only on the magnitude of the loop-current order parameter, but also on the relative phase between the non-zero components of  $\mathbf{L}$  and  $\Phi$ . The second term in Eq. (14) also imposes the constraint  $\Phi_2 = 0$ , otherwise the CDW phase in the orthorhombic phase would spontaneously induce a non-zero magnetic dipole moment (since  $\varepsilon_{xx} \neq \varepsilon_{yy}$ ), which is not observed experimentally. Note that  $\text{sign}(L_1 L_3 \Phi_1 \Phi_3) = -1$  is favored by a positive Landau coefficient  $\kappa_{L\Phi} > 0$  in  $F_{L\Phi}$ , Eq. (3).

The result of this analysis is that the CDW order parameter configuration consistent with the STM experimental observations is the one with  $\mathbf{L} = (L_0, L'_0, L_0)$  and  $\Phi = (\Phi_0, 0, -\Phi_0)$ . From the leading-order couplings to the order parameter  $\mathbf{M}$  in  $F_{LM}$  and  $F_{\Phi M}$ , we also find the subsidiary order  $\mathbf{M} = (M_0, M'_0, M_0)$ , with  $M_0 \sim L_0 L'_0$  and  $M'_0 \sim L_0^2$ . We checked that this configuration results in the magnetic space group *Cmmm* (#65.481), which indeed allows for a non-zero  $\Lambda_{63}$ . We extended this analysis in a systematic way to other configurations of  $\mathbf{L}$  and  $\Phi$ , as shown in the Extended Data Table 1, as well as to cases in which  $\Phi$  transforms as other irreps, but did not find any configurations that lead to an orthorhombic magnetic space group that has  $\Lambda_{63} \neq 0$ .

## Extended References

1. Christensen, M. H., Birol, T., Andersen, B. M. & Fernandes, R. M. Loop currents in  $\text{AV}_3\text{Sb}_5$  kagome metals: Multipolar and toroidal magnetic orders. *Phys. Rev. B* **106**, 144504 (2022).
2. Kautzsch, L. *et al.* Structural evolution of the kagome superconductors  $\text{AV}_3\text{Sb}_5$  ( $\text{A} = \text{K}, \text{Rb}$ , and  $\text{Cs}$ ) through charge density wave order. *Phys. Rev. Mater.* **7**, 024806 (2023).
3. Christensen, M. H., Birol, T., Andersen, B. M. & Fernandes, R. M. Theory of the charge-density wave in  $\text{AV}_3\text{Sb}_5$  kagome metals. *Phys. Rev. B* **104**, 214513 (2021).

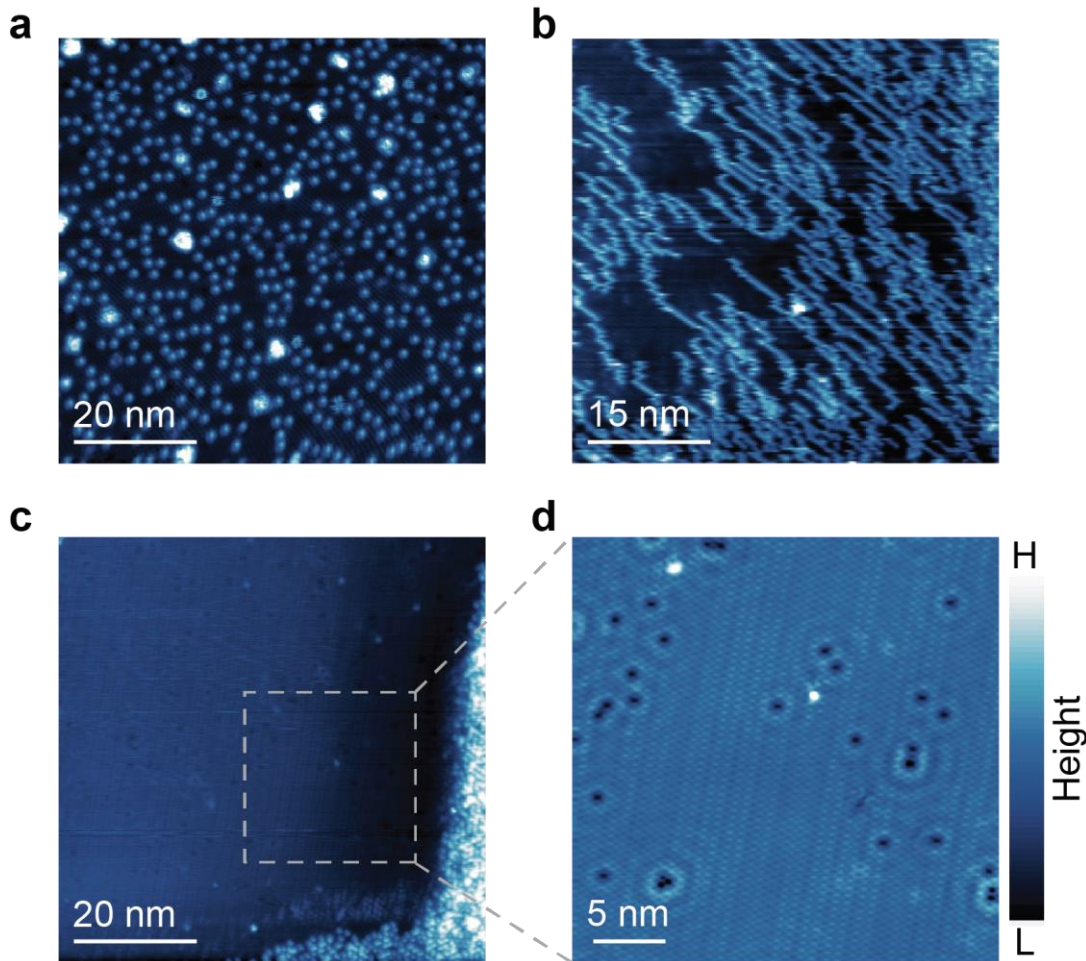
## Extended Data Table 1

$L_2^-$ bond-order CDW	$mM_2^+$ loop-current CDW	Magnetic Space Group	Macroscopic Magnetization	Nonzero Components of Piezomagnetic Tensor
$L_1 = L_2 \neq L_3$	$\Phi_1 = -\Phi_2, \Phi_3 = 0$	$Cmmm$ (#65.481)	none	$yzx = zyx$ $xzy = zxy$ $xyz = yxz$
$L_1 = -L_2, L_3 = 0$	$\Phi_1 = \Phi_2, \Phi_3 = 0$	$C_{Ammm}$ (#65.490)	none	none
$L_1 = -L_2, L_3 = 0$	$\Phi_1 = -\Phi_2, \Phi_3 = 0$	$C_{Accm}$ (#66.500)	none	none
$L_1 = L_2 \neq L_3$	$\Phi_1 = \Phi_2 \neq \Phi_3$ ( $\Phi_3$ may be zero)	$Cm'm'm$ (#65.485)	$M_z$	$xxz$ $yyz$ $zzz$ $yzy = zyy$ $xzx = zxx$
$L_1 \neq L_2 \neq L_3$	$\Phi_1 \neq \Phi_2 \neq \Phi_3$	$P2/m$ (#10.42)	$M_z$	$yyz$ $zzz$ $xxz$ $zxy$ $zxx$ $yxz$ $yzy$ $yzx$

**Extended Data Table 1: Magnetic space groups for different combinations of the bond-order CDW and the loop-current CDW order parameters.**

Of the possibilities considered, only the congruent CDW phase exhibits the required piezomagnetism in the absence of a macroscopic magnetization. Note that the combination of order parameter  $L_1 = L_2 \neq L_3$  and  $\Phi_1 = -\Phi_2 \neq \Phi_3$  with  $\Phi_3 \neq 0$  reduces the symmetry down to monoclinic  $P2/m$ , where none of the order parameters components remain equal.

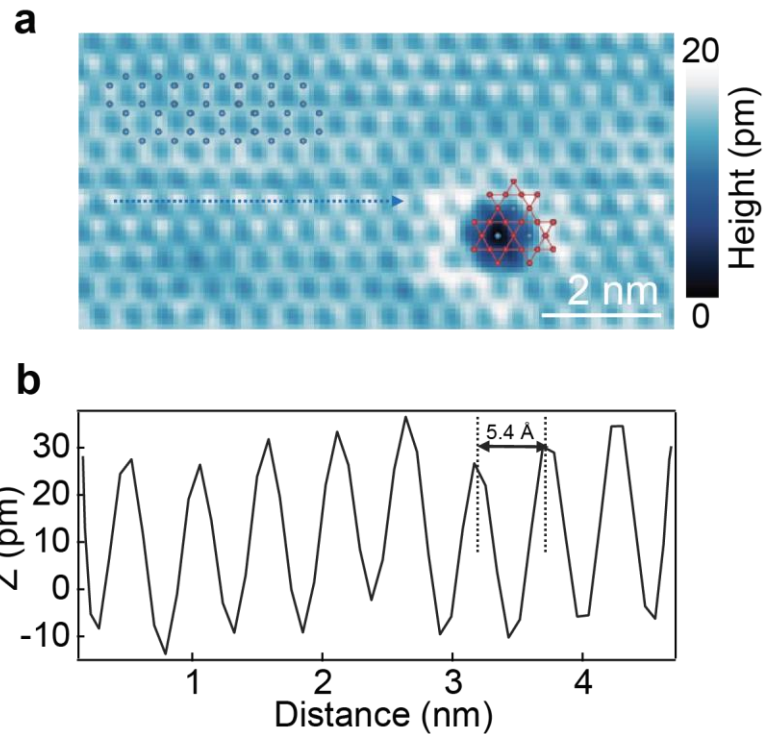
## Extended Data Fig. 1



**Extended Data Fig. 1 | Revealing Sb surface atomically precise sweeping method.**

**a**, Initial topography image (70 nm x 70 nm) showing Sb surface with randomly distributed Rb adatoms on top ( $V_s = -200$  mV;  $I_t = 100$  pA). **b**, 'Sweeping' away surface Rb adatom. moving adatoms show as line shape in topography image ( $V_s = -50$  mV;  $I_t = 1.5$  nA). **c**, After adatom manipulation, all adatoms move to the corner of scan frame (70 nm x 70 nm), exposing clean Sb surface ( $V_s = -100$  mV;  $I_t = 100$  pA). **d**, Zoom-in topography image (30 nm x 30 nm) of dashed square region in (c), showing honeycomb structure of Sb surface ( $V_s = -100$  mV;  $I_t = 500$  pA).

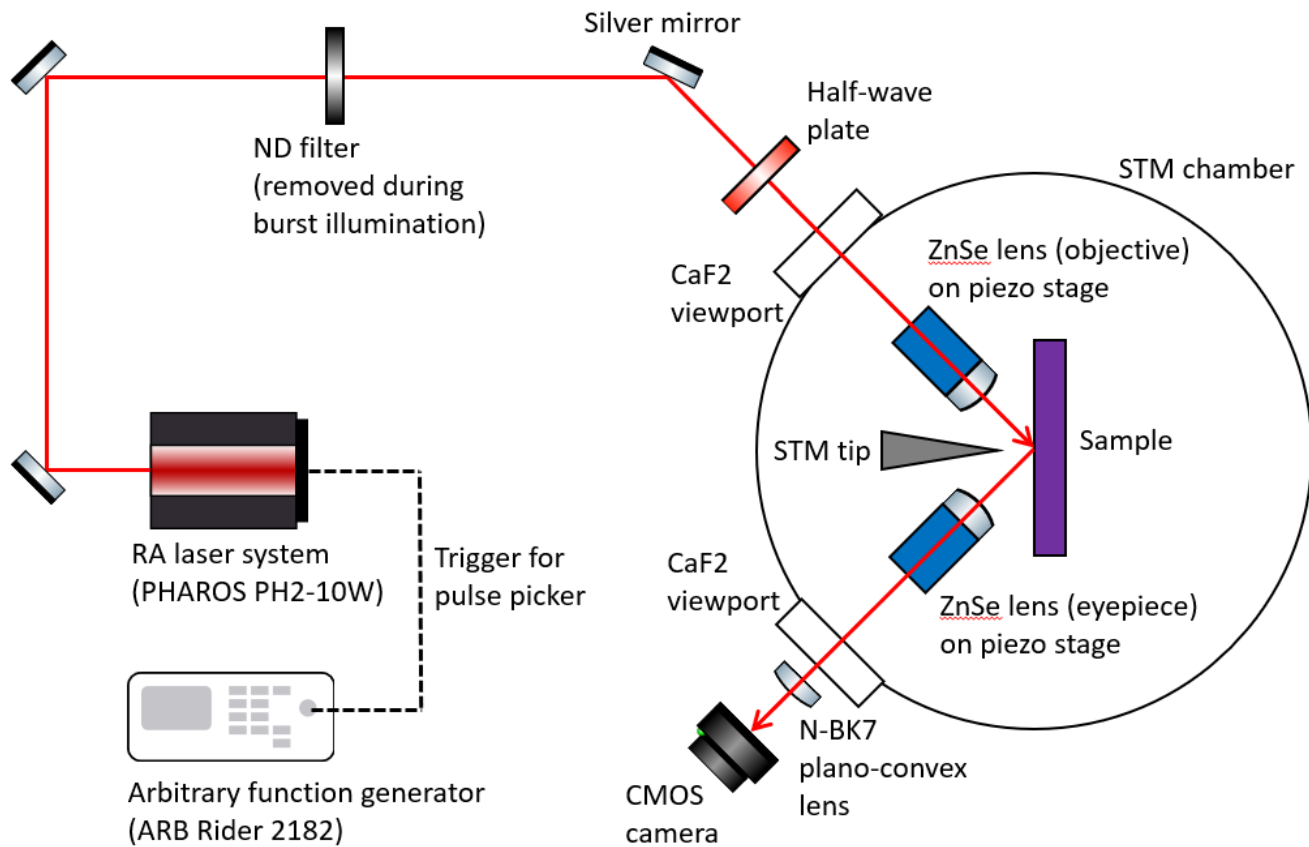
## Extended Data Fig. 2



### Extended Data Fig. 2 | High-resolution topography and lattice constant of Sb layer.

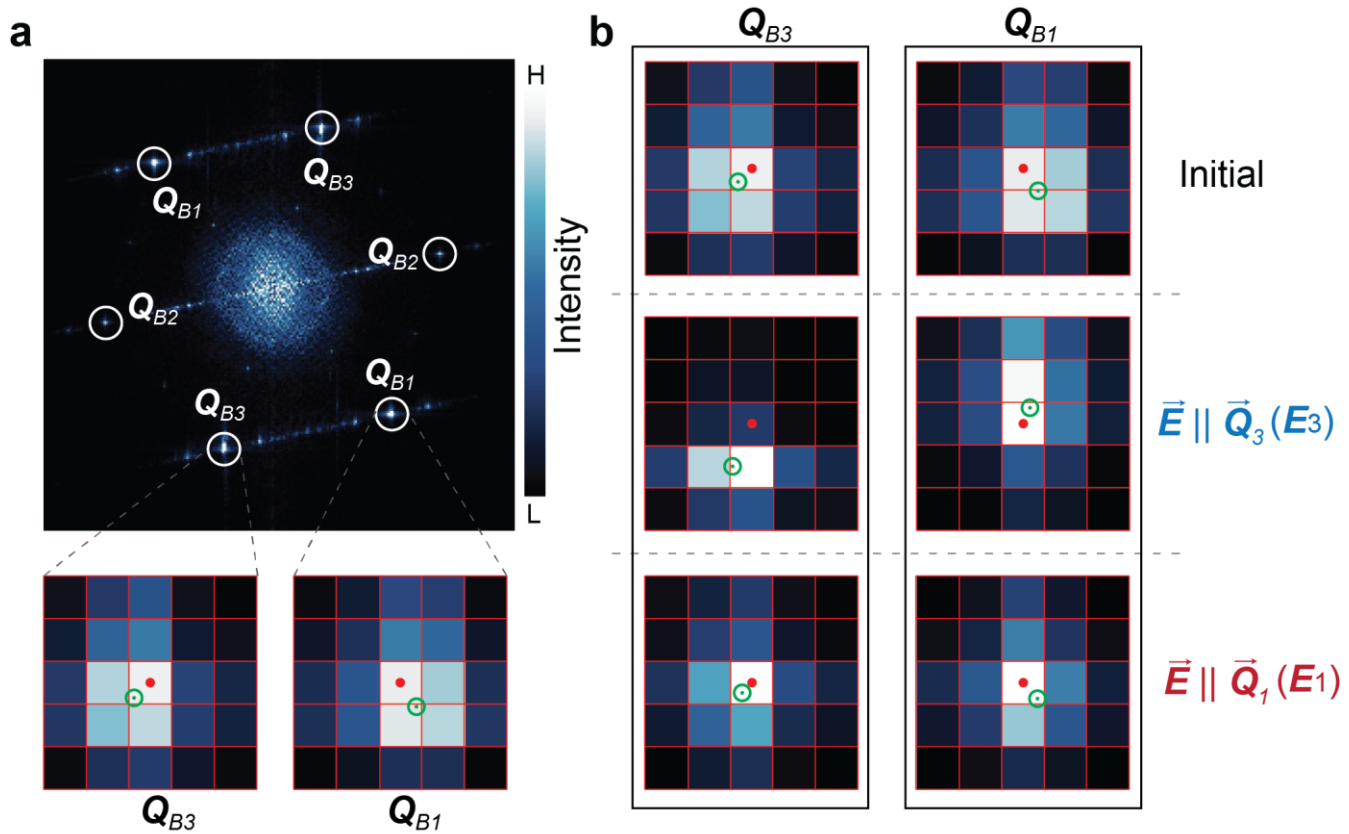
**a**, Atomic-resolution topographic image of Sb lattice ( $V_s = -200$  mV;  $I_t = 100$  pA). Overlapped crystal structures clearly highlight the honeycomb Sb lattice (blue) and underlying kagome V lattice (red). **b**, Line profile of dashed blue arrow in (a), denoting a  $\sim 5.4$  Å surface atomic spacing corresponding to the Sb lattice.

### Extended Data Fig. 3



Extended Data Fig. 3 | Optics layout of the laser-STM setup.

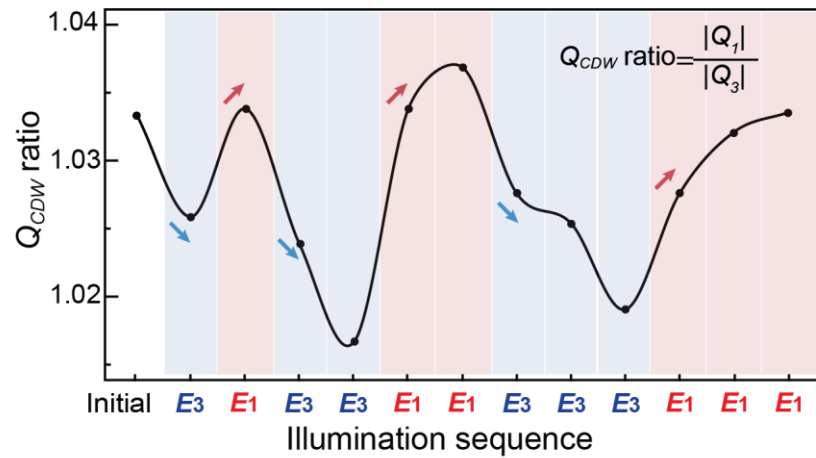
## Extended Data Fig. 4



### Extended Data Fig. 4 | Identification of Bragg peak vector locations.

**a**, Typical FT of the Sb layer before light illumination. Bragg peaks are clearly observed and highlighted with circles. Zoom-in images of these peaks along  $\mathbf{Q}_{B1}$  and  $\mathbf{Q}_{B3}$  directions reveal anisotropic intensity distribution in a 5-pixel x 5-pixel size in momentum space, thus enabling us to carry out the effective center of mass to identify the actual peak location (green circles). **b**,  $\mathbf{Q}_{B1}$  and  $\mathbf{Q}_{B3}$  peak locations during light illumination along either  $\mathbf{E}_1$  or  $\mathbf{E}_3$  directions, showing noticeable extending/shrinking peak location. The red dot in the middle of FT serves as reference for relative peak location change.

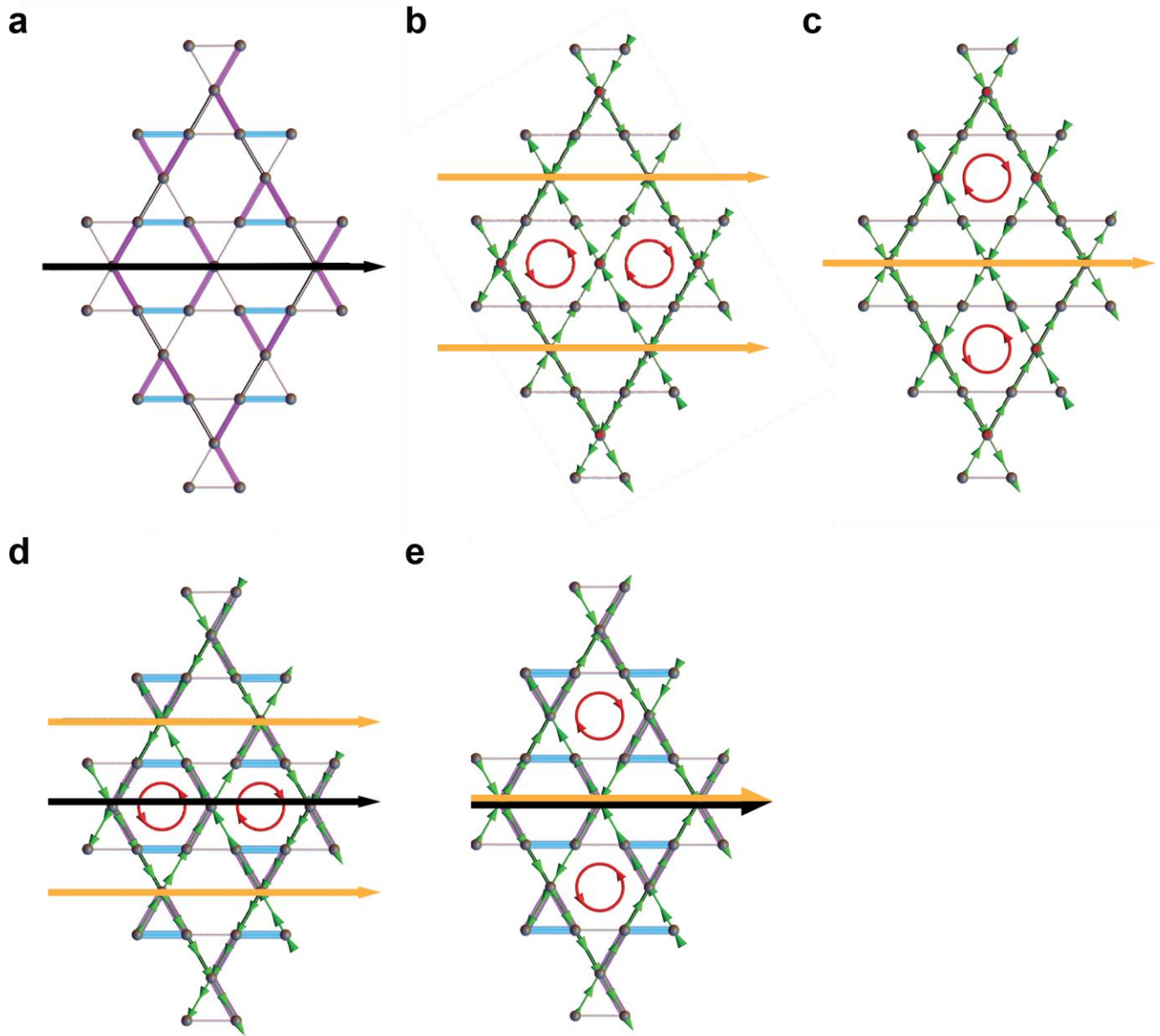
## Extended Data Fig. 5



**Extended Data Fig. 5 | Trend of CDW peak vector ratio between  $Q_1$  and  $Q_3$  for an arbitrary laser illumination sequence.**

During the laser illumination sequence used in Fig. 3a and 3c, the CDW peak ratio shows the same pattern trend as the relative CDW intensity  $I_r$  (Fig. 3a) and  $Q_{Bragg}$  ratio  $Q_r$  (Fig. 3c).

## Extended Data Fig. 6



**Extended Data Fig. 6 | Vanadium bond order and loop current pattern and their rotation axis for different order parameter configurations.**

**a**, Vanadium bond-order pattern (colored bonds) for the 3Q “real” CDW order parameter configuration  $\mathbf{L} = (L, L', L)$  on a single kagome layer. The black line denotes the in-plane 2-fold rotation axis. **b**, Loop-current pattern (green arrows) for the 2Q “imaginary” CDW order parameter configuration  $\Phi = (\Phi, 0, \Phi)$ , whose relative phase between its non-zero

components is trivial. The 2-fold rotation axis is denoted as the orange lines. The closed current loops are denoted as red circles. **c**, Loop-current pattern for the 2Q “imaginary” CDW order parameter configuration  $\Phi = (\phi, 0, -\phi)$ . There exists a relative  $\pi$  phase between the non-zero components, which changes the location of the 2-fold rotation axis. **d**, An overlay view of the  $L_1 = L_3 \neq L_2$  and  $\Phi_1 = \Phi_3$  orderings. In this case, bond-order and loop-current patterns have different rotation axis so that the 2-fold rotation is broken in the system, which allows a macroscopic out-of-plane magnetic dipole moment. **e**, An overlay view of the  $L_1 = L_3 \neq L_2$  and  $\Phi_1 = -\Phi_3$  orderings. In this case, both bond-order and loop-current patterns share the same rotation axis, so that the system possesses an in-plane 2-fold rotation axis, which forbids a magnetic dipole moment. This configuration allows the system to have piezo-magnetic effect even in the absence of a magnetic dipole moment.